Theses and Dissertations

December 2014

The Structure and Ferroelectric Properties of Iron-Doped Lead Titanate

Michael Bartlein
University of Wisconsin-Milwaukee

Follow this and additional works at: https://dc.uwm.edu/etd

Part of the Materials Science and Engineering Commons, and the Physics Commons

THE STRUCTURE AND FERROELECTRIC PROPERTIES OF IRON-DOPED LEAD TITANATE

by

Michael Bartlein

A Thesis Submitted in

Partial Fulfillment of the

Requirements for the Degree of

Master of Science

in Physics

at

The University of Wisconsin-Milwaukee

December 2014

ABSTRACT

THE STRUCTURE AND FERROELECTRIC PROPERTIES OF IRON-DOPED LEAD TITANATE

by

Michael Bartlein

University of Wisconsin-Milwaukee, 2014
Under the Supervision of Professor Marija Gajdardziska-Josifovska
and Professor Prasenjit Guptasarma

Multiferroics are a class of poorly understood, but technologically important materials. Lead(II) titanate ($PbTiO_3$) is a known perovskite ferroelectric. By doping $PbTiO_3$ with Fe^{3+} at the Ti site, we produce the multiferroic $PbTi_{1-x}Fe_xO_3$ (PTFO). Using selected area electron diffraction on a transmission electron microscope, the structure of PTFO is investigated. Of particular interest is identifying the cubic-to-tetragonal transition at the Curie temperature. As the concentration of Fe increases, the crystal becomes more cubic and experiences a lower transition temperature. I also establish a procedure for preparing bulk PTFO samples for ferroelectric testing and present preliminary results establishing ferroelectricity in these PTFO samples. Ferroelectricity is determined by detecting the remanent polarization and switching voltage from ferroelectric hysteresis. A Radiant Technologies Precision LC loop-tracing assembly is used to test the samples for ferroelectric hysteresis.

TABLE OF CONTENTS

LIST OF FIGURES

Chapter 1

Introduction

1.1 Multiferroics and the Linear Magnetoelectric effect

Multiferroics are materials which exhibit coupling between two or more order parameters.

An important subset of multiferroics are magnetoelectrics. Materials that couple ferroelectric ordering with magnetism have applications in electronic switches, sensors and magnetoelectric memory. Magnetoelectrics exhibit co-existing ferroelectric and ferromagnetic (or antiferromagnetic) ground states. The most common mechanism in magnetoelectrics is geometry-driven or type I. Type I multiferroics include the rare earth oxide magnetoelectrics and the complex perovskite oxides, including $PbTi_{1-x}Fe_xO_3$.

Magnetoelectrics are relatively rare in nature [4]. This is due to the conflicting mechanisms that give rise to ferroelectricity and ferromagnetism respectively. In displacive
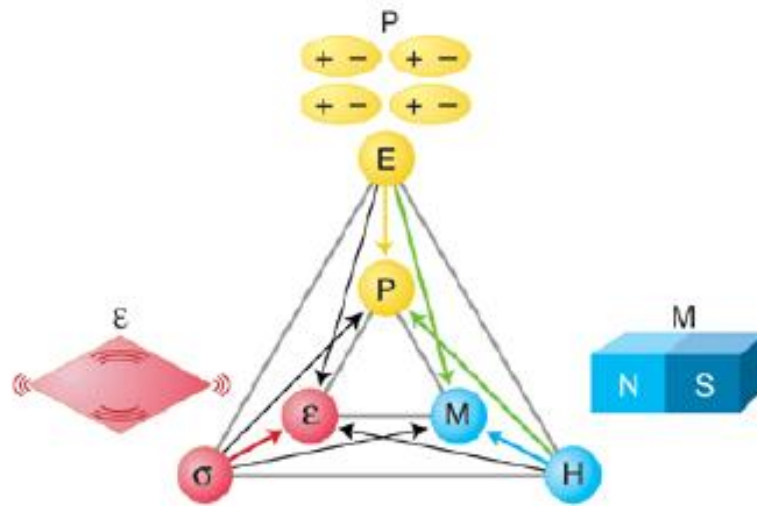
FIGURE 1.1: The couplings between 3 common order paramters (polarization, P, magnetization, M, and strain, ϵ) and external fields (electric field, E, magnetic field, H, and stress, σ) in multiferroics. Reproduced from [1]

perovskite ferroelectrics, the dipole moment is generated from a hybridized bond between the B site ion, typically a transition metal (Ti^{4+}, Mn^{3+}, Zr^{4+}) and the oxygen octohedra. This bond requires an empty d-orbital in the B site ion i.e. d^0-ness. This is due to the interaction between a postively charged transition metal ion and the negatively charged ligands around it [5]. In a perovskite structure, six ligands (Oxygen in the case of $PbTi_{1-x}Fe_xO_3$) are arranged in a octohedron around the ion. In octohedral symmetry, there is a spatial degeneracy in the d-orbital. This degeneracy is removed via a hybridized bond between the p-orbital of the O octohedra and the empty p orbital. However, a d^0 ion has no unpaired electron, and thus no net spin that would impart a magnetic moment on the ion. This generally prohibits ferromagnetism (or antiferromagnetism) in systems with d^0 B site ions. Thus, displacive ferroelectrics such as $PbTiO_3$ rarely have a simultaneous magnetic moment. [6]

1.2 Landau-Devonshire Theory

A successful theory of ferroelectricity is provided by Landau-Devonshire theory [7]. The treatment given here is based off of Kardar [8].

Consider the Landau free energy density, $\mathcal{F}$ of a ferroelectric system in a local electric field, E. Let $\mathcal{F}$ be a function of the scalar order parameter P, the polarization. We can expand about $P = 0$ with a taylor series in P:

$$\mathcal{F} = F_0 + \frac{1}{2}aP^2 + \frac{1}{4}bP^4 + \frac{1}{6}cP^6 - EP \tag{1.1}$$

Although not suitable for all ferroelectric systems, we truncate the series at P^6, which will be suitable to describe many systems. The equilibrium polarization(s) is found by minimizing $\mathcal{F}$

$$\frac{d\mathcal{F}}{dP} = 0 \tag{1.2}$$

$$aP + bP^3 + cP^5 - E = 0 \tag{1.3}$$

Landau-Devonshire theory assumes that a is linear in temperature, T, near the Curie point, T_c:

$$a = \gamma(T - T_0) \tag{1.4}$$

If we take the other coefficients in the expansion to be independent of temperature, then 1.3 becomes:

$$E = \gamma(T - T_c)P + bP^3 + cP^5 \tag{1.5}$$

The dielectric susceptibility (above T_c), given by $\chi = \frac{P}{E}$ can be found by differentiating 1.5 with respect to P at $P = 0$:

$$\chi = \frac{1}{\gamma(T - T_c)} \tag{1.6}$$

Which is consistent with the predicted Curie-Wiess behavior of χ.

a is positive for all known ferroelectrics, as is c [9]. However, the sign of b can be positive or negative. The sign of b determines the order of the ferroelectric transition. If we assume $b > 0$, then the transition at $T = T_0$ is second-order. Setting $E = 0$ and neglecting the P^6 term, we can find the spontaneous polarization, P_0

$$0 = \gamma(T - T_c)P_0 + bP_0^3 \tag{1.7}$$

This has solutions

$$P_0 = 0 \tag{1.8}$$

$$P_0 = \sqrt{\frac{\gamma}{b}(T - T_c)} \tag{1.9}$$

Corresponding to $T > T_c$ and $T < T_c$ respectively.
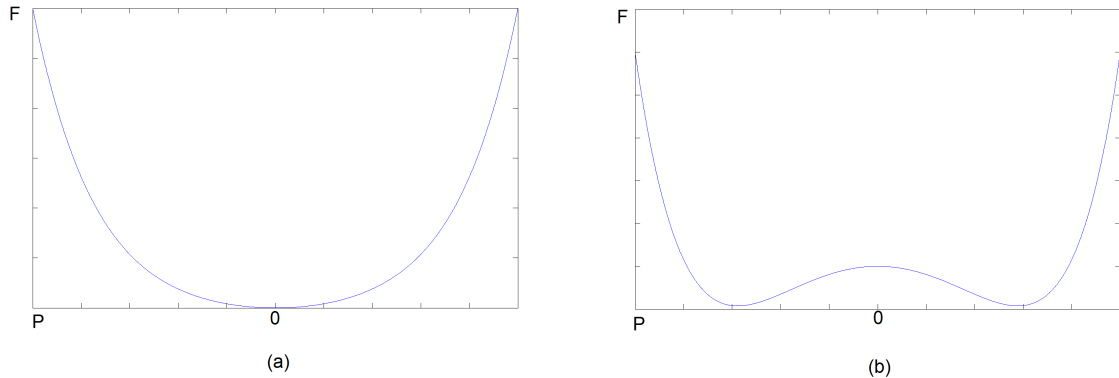
FIGURE 1.2: Free energy as a function of Polarization a) at $T > T_c$ and b) $T < T_c$. The double wells have minima at $\pm P_0$.

1.3 Displacive Ferroelectrics

Many ferroelectrics, including PTO, are undergo a phase transition below T_c in the form of a structural distortion [10]. The ferroelectric ordering in these displacive ferroelectrics is coupled to strain in the lattice [10]. The displacement, $\mathbf{u}$, depends on the strain acting on the lattice. The strain reflects how displacement varies with position in the lattice. The strain is a 3x3 tensor denoted by ϵ

$$\epsilon_{ij} = \frac{1}{2}\left(\frac{\partial u_i}{\partial r_j} + \frac{\partial u_j}{\partial r_i}\right) \tag{1.10}$$

Where i, j denote the x, y and z components of the vectors. In the case of ferroelectrics such as $BaTiO_3$ or $PbTiO_3$, this strain is uniaxial (displacement only occurs along the c lattice parameter. We can then write the leading order terms of the free energy

$$\mathcal{F}_\epsilon = \frac{1}{2}K\epsilon^2 + Q\epsilon P^2 + ... - \epsilon\sigma \tag{1.11}$$

Here, the lowest order coupling between strain and polarization is ϵP^2 due to symmetry. K and Q are the elastic constant and coupling term respectively. The full free energy term is now $\mathcal{F} = \mathcal{F}_P + \mathcal{F}_\epsilon$. Minimizing gives

$$\frac{\partial \mathcal{F}(\mathcal{P}, \epsilon)}{\partial P} = \frac{\partial \mathcal{F}(\mathcal{P}, \epsilon)}{\partial \epsilon} = 0 \tag{1.12}$$

From the second equation

$$\frac{\partial \mathcal{F}(\mathcal{P}, \epsilon)}{\partial \epsilon} = K\epsilon + QP^2 - \sigma \tag{1.13}$$

In the case of zero external stresses ($\sigma = 0$), we get

$$\epsilon = -\frac{QP^2}{K} \tag{1.14}$$

This is the tetragonal strain present in displacive ferroelectrics such as $PbTiO_3$ [10] [11]. In $PbTiO_3$, this strain produces a distortion from a cubic to tetragonal lattice. Rather

than calculating ϵ directly, we use c/a the ratio of the long lattice paramter c, and the shorter a as a measure of strain.

1.4 Perovskite Ferroelectrics and $\mathbf{PbTi}_{1-x}\mathbf{Fe}_x\mathbf{O}_3$

An important class of ferroelectrics are the perovskite family of displacive ferroelectrics. Perovskites are composed of ABO_3 type unit cells. As shown in 1.3, the perovskite strucutre consists of a cubic A-site cation with face-centered Oxygen sites forming an octohedron. In the center of the unit cell is a B-site cation. Displacement of the B-site from a centrosymmetric position gives rise to a dipole moment in the perovskite unit cell, for example the systems $BaTiO_3$ and $PbTiO_3$. This distortion is the cause of ferro-electricity in the perovskite ferroelectrics, and is due to hybridized bonding between the B site $3d$ and the O site $2p$ orbitals [12]. Most ferroelectric perovskites have B site ions with unoccupied d orbitals (ex. Ti^{4+}, with an electron configuration $[Ar]3d^0$), which allows for a stable hybridized bond with the apical O site [12].

The ferroelectric transition in perovskites are correlated with a structural transition. In the case of $PbTiO_3$, the system is a cubic lattice above the Curie point ($T_c = 766K$). This transitions to a tetragonal phase (lattice constants $a = b \neq c$) below the Curie point. $PbTiO_3$ has a comparatively large tetragonal distortion, $c/a = 1.06$ [1] [13]. This ferroelastic behavior is expected due to the strain along the c axis from the displaced Ti^{4+} ion. Lattice distortions do not necessarily only occur along one axis. The well known ferroelectric PZT is known is be monoclinic below T_c [14][15], and some sources
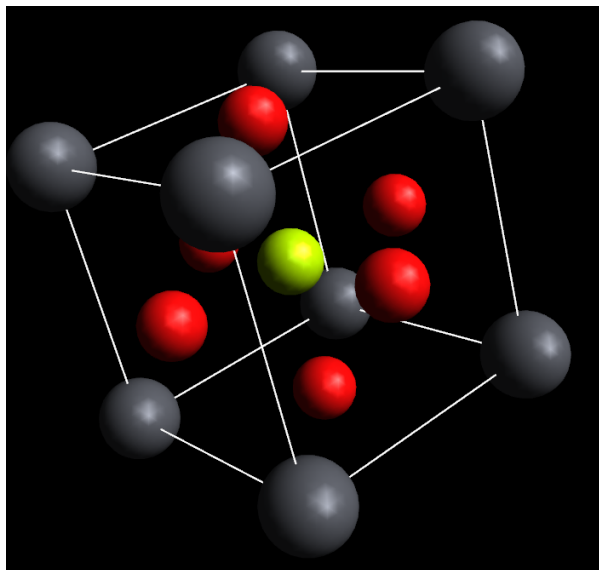
FIGURE 1.3: The ABO_3 perovskite strucuture of lead titanate (grey = Pb, red = O, green - Ti).

have found distortion along the b parameter in PTO as well [16]. However, if present, the non-tetragonal distortion in PTO is slight, and will not be addressed in this work.
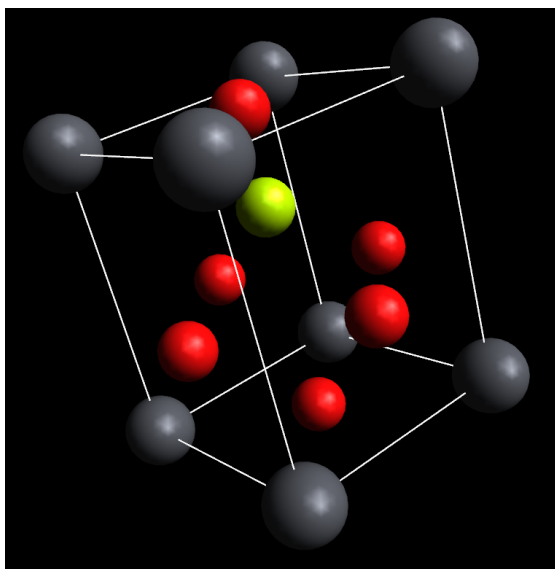
FIGURE 1.4: lead titanate in the tetragonal phase. Note the displaced Ti and O atoms, leading to the dipole moment.

When $PbTiO_3$ is doped with Fe^{3+} at the B site to create $PbTi_{1-x}Fe_xO_3$, the c/a ratio

of the system decreases. This is likely due to Fe^{3+} lacking "d^0-ness", thus reducing or eliminating the displacive bonding between the B site and O site ions [5]. The substitution of Iron in the perovskite lattice is designed to introduce a ferromagnetic ordering to the system.

Chapter 2

Electron Diffraction study of Structural Transition in $\mathbf{PbTi_{1-x}Fe_xO_3}$

In this chapter, I will present the crystal symmetry and lattice constants of $PbTi_{1-x}Fe_xO_3$ at $x = 0.1$ and $x = 0.5$, and the structural transition from a tetragonal perovskite lattice below the Curie temperature to a cubic perovskite above it. By establishing the transition temperature and tetragonality (measured as the ratio c/a) as a function of x, the effect of iron doping on ferroelectric ordering in lead titanate can be established. The $x = 0$ lattice parameters are also presented as a good reference point, as the lattice parameters of $PbTiO_3$ are well established [13] [16] [17].

2.1 Electron Diffraction

Analysis of the $PbTi_{1-x}Fe_xO_3$ samples are done using electron diffraction in a transmission electron microscope. Electron diffraction relies on the wave nature of electrons to scatter through a crystal lattice, much like x-ray diffraction. The wavelength of the scattering electron is given by De Broglie [18]:

$$\lambda = h/p \tag{2.1}$$

When the electron is accelerated through a potential, eV, it gains kinetic energy:

$$\frac{1}{2}mv^2 = eV \sqrt{2meV} = mv = p \tag{2.2}$$

The relativistically correct form of the electron's wavelength becomes:

$$\lambda = \sqrt{\frac{h^2c^2}{eV\left(2m_0c^2 + eV\right)}} \tag{2.3}$$

Where m_0 is the rest mass of the electron ($m_0 = 9.11 * 10^{-31}$ kg). The wavelength of an electron undergoing an acceleration voltage of 300 keV is approximately $\lambda = 1.97$ pm. For reference, an X-ray has a wavelength on the order of 100 pm.

How an electron wave will scatter from a crystal is determined by Bragg's law [19]:

$$n\lambda = 2d\sin\theta_B \tag{2.4}$$

Where d is the interplanar spacing of the crystal and θ_B is the Bragg angle. At the Bragg angle the electron waves interfere constructively (Figure 2.1). It is important to note that although Bragg's law is derived for reflections off a lattice, the result is valid for electron diffraction, where the waves are transmitted through an electron transparent material [18].

To interperate diffraction pattern's it is helpful to rewrite Bragg's law in terms of the wavevector, $\mathbf{k}$. Let the difference between the incident wavevector and the diffracted wavevector is:

$$\mathbf{K} = \mathbf{k}_D - \mathbf{k}_I \tag{2.5}$$

Using the fact that the magnitude of the wavevector is the reciprocal of the electron wavelength:

$$\frac{1}{\lambda} = |\mathbf{k}| \tag{2.6}$$

Bragg's law can be rewritten in terms of $\mathbf{K}$:

$$|\mathbf{K}| = \frac{2\sin\theta}{\lambda} \tag{2.7}$$

We define the wavevector when $\theta = \theta_B$ as the reciprocal vector, $\mathbf{g}$. Crucially, diffraction through a crystal willl occur along crystal planes. Therefore, we can associate each

reciprocal vector with a crystal plane:

$$\mathbf{g}_{hkl} = h\mathbf{a}^* + k\mathbf{b}^* + l\mathbf{c}^* \tag{2.8}$$

Where hkl is the miller index of the lattice plane and $\mathbf{a}^*$, $\mathbf{b}^*$ and $\mathbf{c}^*$ are unit cell translations in reciprical space. We can then relate $\mathbf{g}$ to the interplanar spacing of the lattice, and therefore relate the locations of the diffraction peaks in the diffraction pattern to the lattice parameters of the crystal.

$$d_{hkl} = \frac{1}{|\mathbf{g}|} \tag{2.9}$$

From the electron diffraction pattern, the d-spacing is calculated from the distance of the hkl peak, R_{hkl}, from the central (000) peak.

$$d_{hkl} = \frac{\lambda L}{R_{hkl}} \tag{2.10}$$

Where L is the effective camera length, the distance between the specimen plane and image plane, accounting for the intermediate and projector lenses. For a tetragonal lattices $(a = b \neq c)$, the relationship between the interplanar spacing and the lattice parameters is [19]

$$d_{hkl}^2 = \frac{a^2}{h^2 + k^2} + \frac{c^2}{l^2} \tag{2.11}$$

The result is a diffraction pattern of bright peaks where the bragg condition is satisfied.
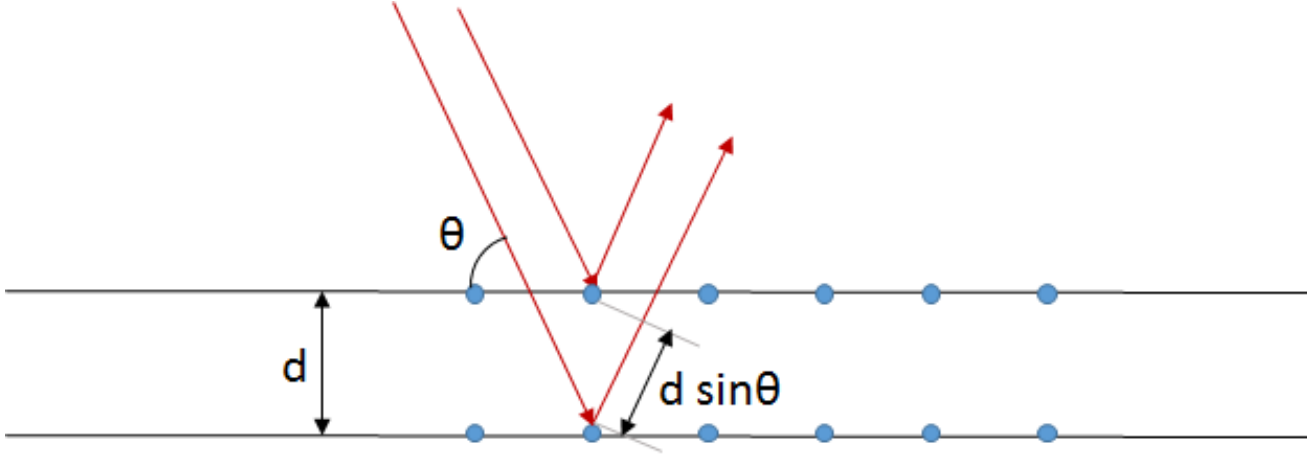
FIGURE 2.1: An illustration of Bragg's law. The two incident waves are scattered at the Bragg angle, so that the phase shift is λ and constructive interference occurs.

The diffraction patterns shown in this chapter are multicrystaline, or powder diffraction patterns, where the orientations of the crystals in the selected area are randomly distributed. In these patterns, the peaks from the combined crystal orientations form a ring with radius $|\mathbf{g}|$.

The lattice parameters can then be calculated for the (200) peak, for instance:

$$d_{200} = \frac{\lambda L}{R_{200}} \tag{2.12}$$

$$d_{200}^2 = \frac{a^2}{4} \tag{2.13}$$

$$a = \frac{2\lambda L}{R_{200}} \tag{2.14}$$

First, the reciprocal vector magnitude is measured from the distance from the (000) peak to the (200) peak in the diffraction pattern. Then, the lattice parameter a is calculated.

For a cubic structure ($a = b = c$), such as PTFO above T_c, many miller indices share the same reciprocal vector magnitude. Continuing with the above example, the (200), (020),

and (002) rings are degenerate in the cubic phase. In the tetragonal phase, however, the peaks "split" since $d_{200} \neq d_{002}$. The ratio c/a, as noted in Chapter 1, is used as a measure of tetragonality.

2.2   Experimental Setup

The PTFO samples are produced by a modified Pechini solution-gelation process. The Pechini method requires combining metal salts with citric acid and ethylene glycol and involves two main reactions. The first is the chelation of the metal ions with citric acid. The second is the formation of a viscous When heated or exposed to vacuum, the polyester liquid dries into a polymer gel. The proper ratio of citric acid to ethylene glycol is required for the formation of the gel. Upon calcination at or above $100°$, this gel dries into the final metal oxide powder. [17]

The source of Ti, Fe and Pb ions are provided by solutions of Lead(II) Nitrate (99.999%), di-hydroxy bis (50%) and Iron(III) nitrate nonahydrate (98-101%) from Alfa Aesar Puratronic. The gelation agent is citric acid stabilized with ethylene glycol. Chelation between the metal ions and the acid produces a viscous polymeric resin. The gel is heated to form a transparent thermoplastic, then the sample is pulverized, mixed and calcinated at $600°$ C for 2 hours. The sample is then annealed at $600-650°$ C for up to 12 hours. The resulting PTFO is a single phase multicrystal with crystal size between 20-50nm [16].

For analysis under the electron microscope, $PbTi_{1-x}Fe_xO_3$ sample was deposited on 2mm Cu specimen grids with either lacey carbon or ultrathin carbon support films. The samples were deposited using a colloidal solution of methanol and $PbTi_{1-x}Fe_xO_3$. The grids were placed inside a dessicator for at least 24 hours prior to placing in the microscope. Samples are characterized using a Hitachi H-9000NAR Transmission Electron Microscope with a 300keV beam. To determine the lattice parameters of the sample, selected area diffraction (SAD) of a multicrystalline sample region of approximately $1\mu m$ was used during *in situ* heating. The imaged samples are multicrystalline groups of $PbTi_{1-x}Fe_xO_3$. Since the samples consist of many random orientations, diffraction produces a ring pattern. Diffraction patterns were taken at roughly 25°C intervals, from room temperature (26°C) to 548°C. Unless otherwise noted, all diffraction patterns were taken at a camera length of 0.25cm.

An Orius 2408x2408 pixel CCD camera operated on Gatan Digital Micrograph was used to record all images and diffraction patterns on the TEM. Figure 2.3 shows the diffraction pattern of PTFO $x = 0.5$ taken at 25°C. When selecting a sample area for SAD, the highest quality, "smoothest" diffraction patterns will be produced from dense clusters. Figure 2.2 shows the sample area of $PbTi_{0.9}Fe_{0.1}O_3$. Using bright field imaging of the selected diffraction area verifies the sample crystal sizes to be between 20-50nm. I used the DiffTools tool suite to produce rotational average intensity profiles of the powdered diffraction patterns.

Diffraction peaks were fitted using an iterative least-squares algorithm in MagicPlot. Figure 2.4 shows the intensity profile in the MagicPlot GUI. Initial gaussian "guess"
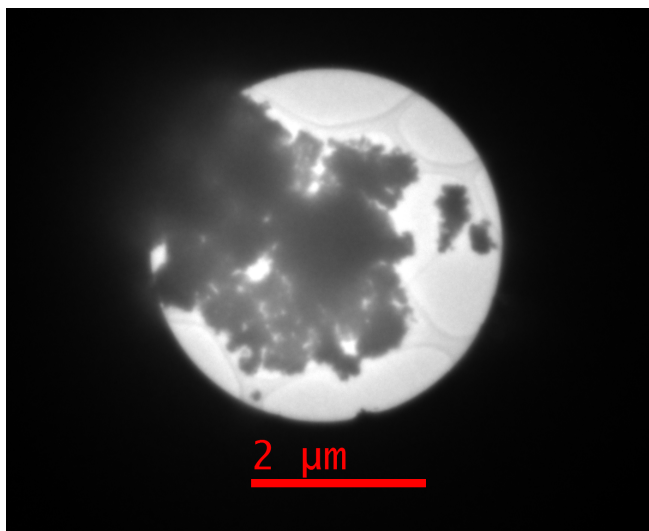
FIGURE 2.2: Sample area of PbTi$_{0.9}$Fe$_{0.1}$O$_3$ at 1k magnification. The area is imaged with the 4.014 μm diameter selected area aperature.
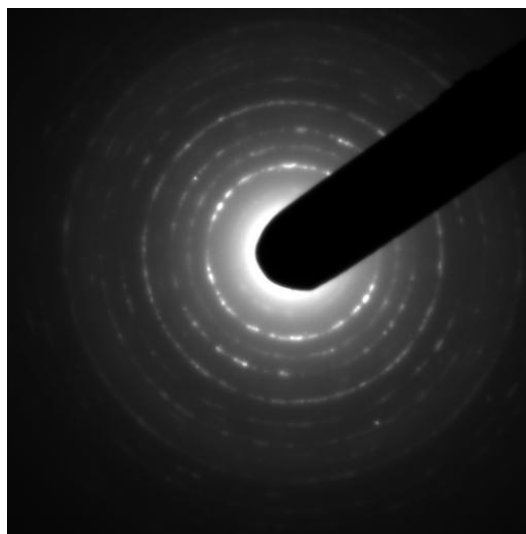
FIGURE 2.3: SAD pattern of PbTi$_{0.5}$Fe$_{0.5}$O$_3$ at 25$^\circ C$ and a camera lenght of 0.25m. This pattern indicates a cubic or nearly-cubic structure.

peaks are provided by the user. To take advantage of twofold peak splitting in the tetragonal regime, the 200 and 002 peaks are fitted lorentzian curves. Each pair of curves have their half width half maximum parameters set equal. The HWHM of the fit curves are set equal in order to reduce the tendecy to fit both peaks using a single curve

in almost-cubic profiles, with the second curve almost nonexistant or set far outside of the peak, so that only the gaussian tail contributes to the fit.
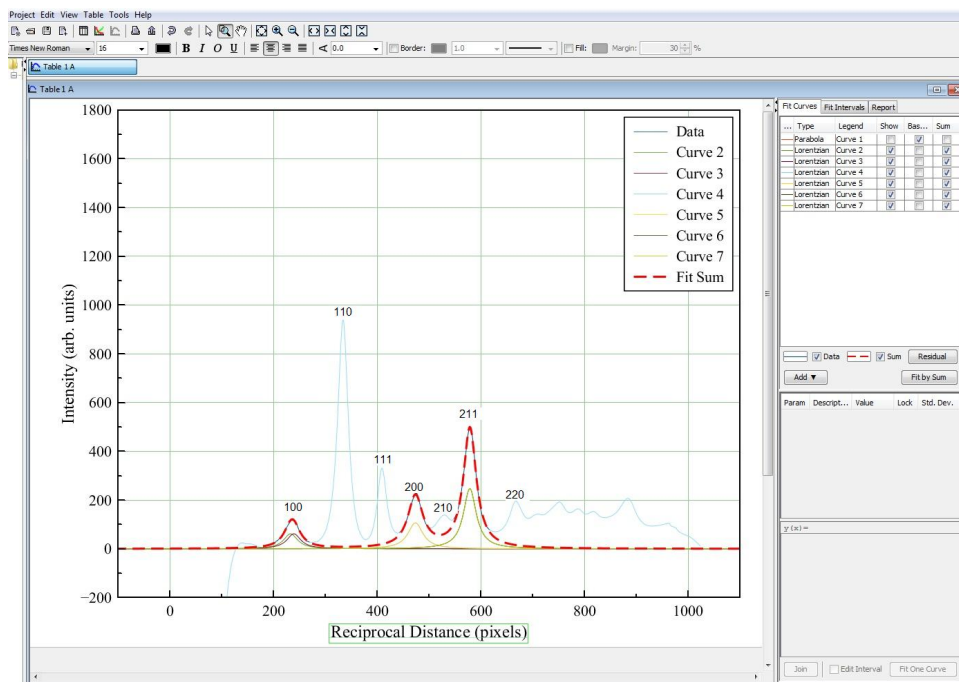
FIGURE 2.4: The MagicPlot software with a diffraction profile being fitted using lorentzian curves on the 100, 200 and 211 peaks.

2.3   Results and Discussion

Producing an inensity profile from a diffraction pattern using the DiffTools suite requires defining the center of the pattern, that is the center of the 000 peak. The lack of angular symmetry due to the beam stop in the diffraction pattern means that I centered the images manually, using visual centering aids provided in DiffTools. Because this step in determining the lattice parameters is done with a human making visual judgments, a degree of of error is introduced independent of the least squares fitting algorithm. A

rotationally averaged intensity profile will show broadened peaks if the averaging is done off-center.
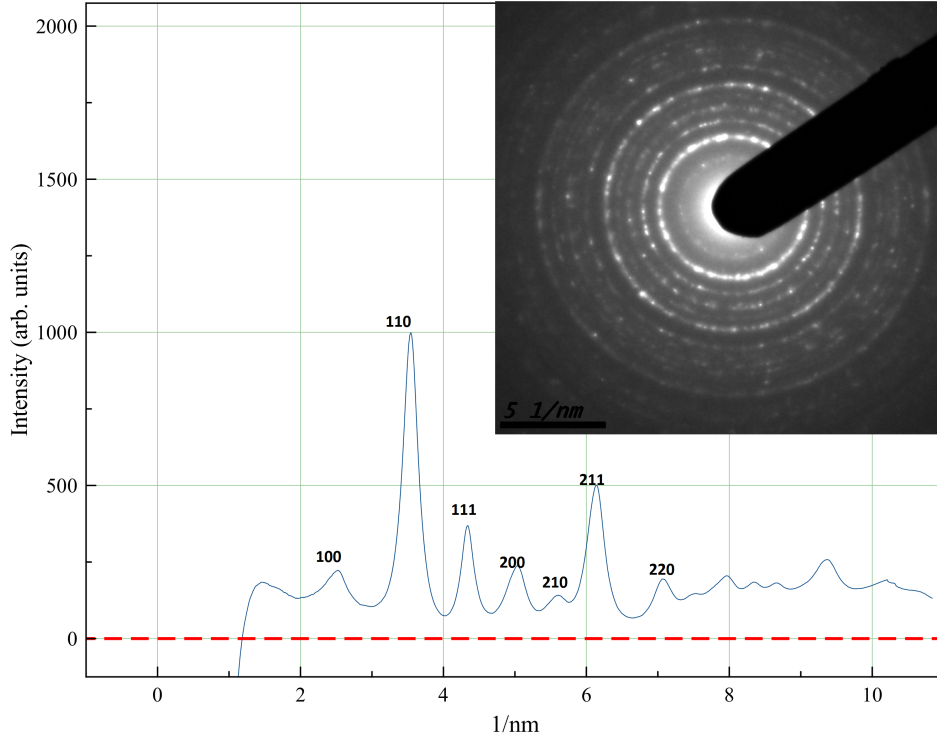
FIGURE 2.5: Indexed intensity profile (inset: TEM diffractogram) of $PbTi_{1-x}Fe_xO_3$ $x = 0.1$ at room temperature ($25°C$). There is evident peak splitting in the 100 and 200 peaks due to the tetragonal phase of PTFO.

Using the fitted peak locations, especially the pronounced split in the (200) and (002) peak in the tetragonal phase, we can calculate c/a ratios at each temperature point in the series. As seen in 2.9, c/a decreases as we approach the Curie temperature. For highly cubic profiles, only the 200 and 002 peaks can be distinguished by the fitting algorithm.

The $PbTi_{0.9}Fe_{0.1}O_3$ lattice parameters are in good agreement with literature values [20] [16]. The c/a ratio decreases from $c/a = 1.045$ at $25°$ C to a nearly cubic $c/a = 1.003$ at $450°$ C. Although the error is too large to pinpoint the Curie temperature precisely,
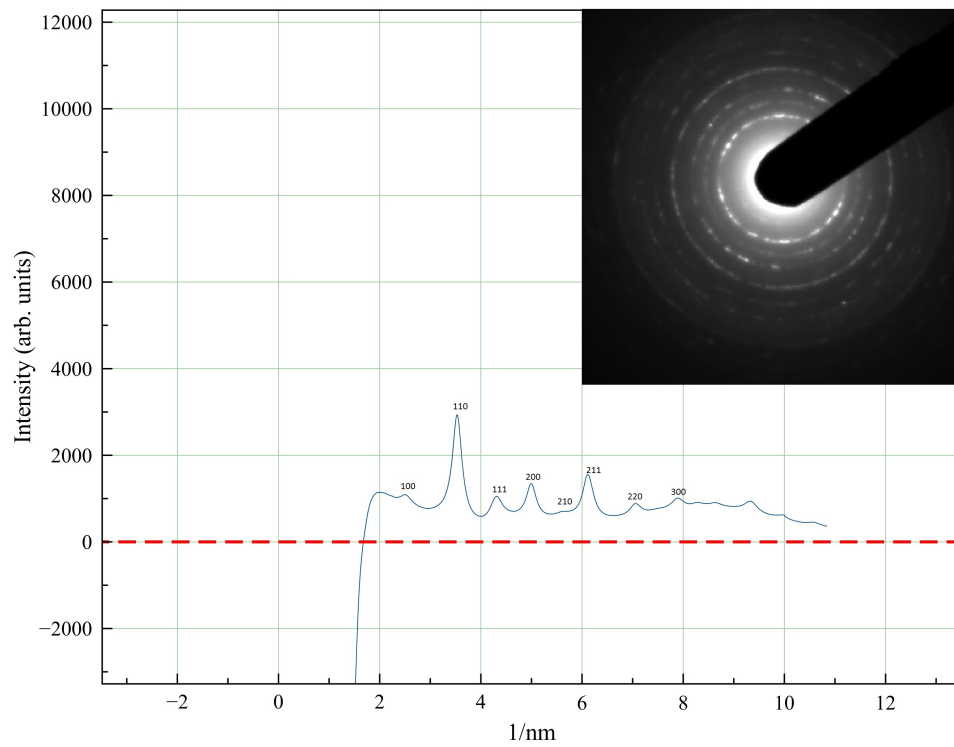
FIGURE 2.6: Indexed intensity profile (inset: TEM diffraction pattern) of PbTi$_{0.5}$Fe$_{0.5}$O$_3$ at room temperature (25°C).
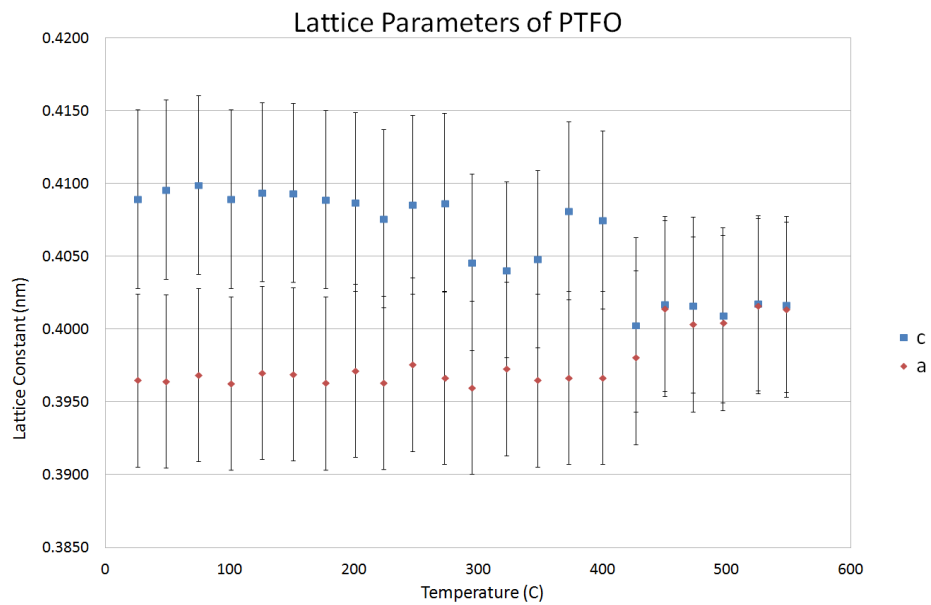
FIGURE 2.7: Lattice parameters for PbTi$_{0.9}$Fe$_{0.1}$O$_3$ as a function of temperature, showing the tetragonal-to-cubic transition.
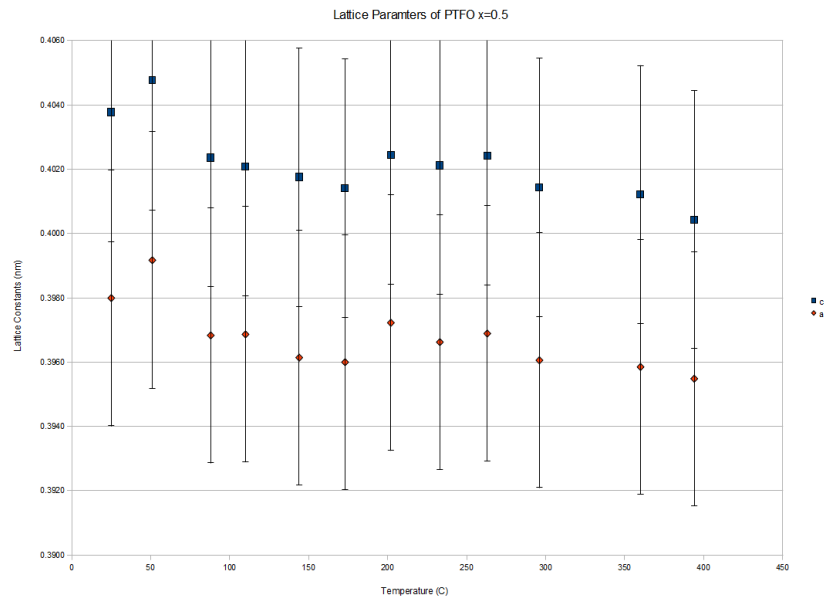
FIGURE 2.8: Lattice parameters for $PbTi_{0.5}Fe_{0.5}O_3$ as a function of temperature.
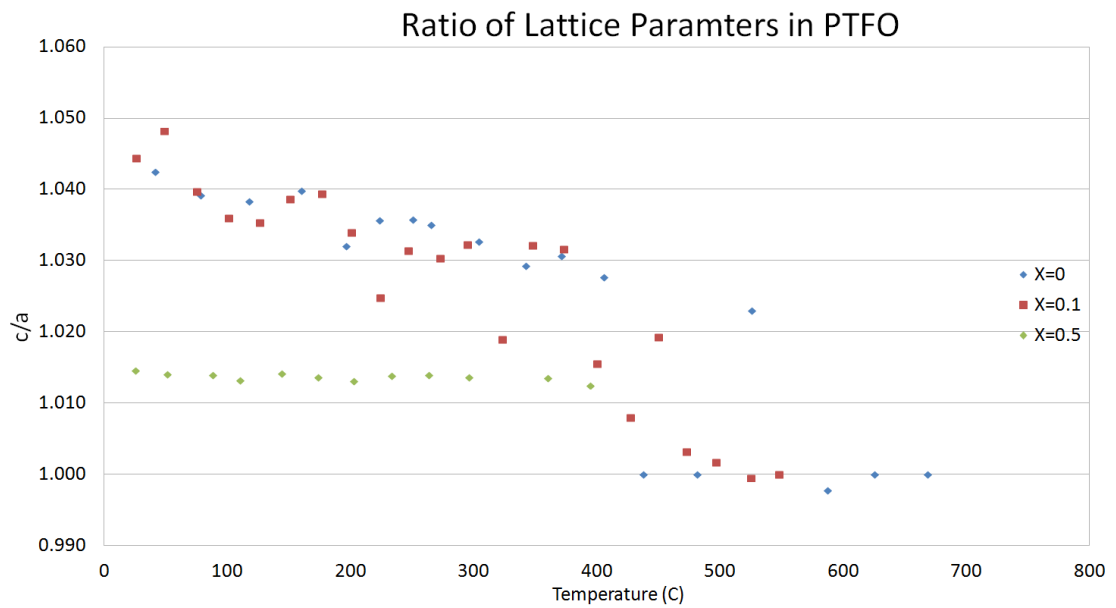
FIGURE 2.9: The c/a ratios for PTFO x=0, x=0.1 and x=0.5 as a function of temperature.

450° C is an entirely reasonable result, consistent with the predicted decrease in T_c from the $x = 0$ value of $T_c = 490°$ [21] [22].

The $PbTi_{0.5}Fe_{0.5}O_3$ set was more problematic. At room temperature, the lattice paramters were found to be $c = 0.4039$ nm and $a = 0.398$ nm, however the errors in these measurements are almost as large as their splitting, suggesting that the diffraction pattern profile lacks the resolution necessary to distinguish the 200 and the 002 peaks consistently.

The high uncertainty present in the lattice parameter calculations make the identification of the Curie temperature problematic. There is a clear transition to a cubic phase near $450°$ C in the $x = 0.1$ and $x = 0$ sample, but no transistion is observed in the $x = 0.5$ sample.

The lack of a noticable transistion in $x = 0.5$ could be due to the experiment not reaching temperature T_c or above. Another distinct possibility is that the 200 and 002 peaks are too close to be fit near T_c and that the tetragonality present in the fit is a result of overfitting the data with two peaks rather than one.

There are several sources of error present in the measurement of lattice parameters. In multicrystalline samples, crystals may lie above or below one another, or vary in thicknesses, resulting in error in the camera length [23]. A significant source of error, as discussed above, is the broadened diffraction peak profile that occures if a diffraction pattern is not cenetered before taking a rotational average. A careful user can visually etstablish the center of a diffraction pattern to within ± 5 pixels. This translates into a shift of 0.004nm in the 200 peak, or an error of about 1%.

Another source of error is variations in fitting parameters, such as the fit interval and the initial guess fit. Experimentation with the fit interval shows a variation of 0.1% in the lattice constants. The initial guess can become problematic, especially for highly cubic

structures. Small changes in initial curves can lead to completely different fits. Usually, an inappropriate fit is immediately obvious to the user, but correcting this fit requires manual adjusting of the fitting parameters. This inevitably introduces user error into the fit.

Ultimately, the error in the lattice parameter fits is difficult to calculate precisely. Measurement error of lattice constants with electron diffraction can be as low as 0.1% [23], but is more typically $1\% - 2\%$. Compounded with uncertainty in peak fitting, the net error is likely between $2\% - 3\%$.

2.4   Conclusion

By measuring the lattice constants *in situ* as a function of temperature, the effect of Fe^{3+} concentration on the Curie temperature and tetragonal displacement in PTFO can be measured. We calculate the lattice constants by fitting the bragg peaks of elecron diffraction images of the sample. By using a TEM to image the sample, we can also verify the size of the sample crystals.

I have shown the lattice parameters measured for $PbTi_{1-x}Fe_xO_3$, $x = 0$, $x = 0.1$ and $x = 0.5$. A tetragonal to cubic transition is shown near $490°$ C for the $x = 0$ sample and $450°$ C for the $x = 0.1$ sample. The $x = 0.5$ sample failed to show a significant reduction in tetragonality as a function of temperature. This may be due to the peak splitting in the 200-002 peak being too small to adequately fit. The reduction of T_c and c/a in the samples as dopant concentration increases suggests the presence of iron in the lattice reduces the ferroelectric phase, and therefore the strain, on the lattice.

By measuring tetragonality of PTFO samples at different concentrations of the dopant Fe, we can observe the magnitude of the displacement of the B site cation. As a "d^0" ion, Ti^{4+} forms an asymmetric bond with an octohedral Oxygen, forming a dipole. The lessening of this displacment, as measured with c/a with the increasing concentration of Fe, indicates a reduction in this displacive bond. Since Fe^{3+} has a partially filled d orbital, it will not make a displacive bond with an Oxygen, reducing the displacive ferroelectric phase [4]. Although, c/a is reduced as x increases, even at $x = 0$, the sample still had a small, but measurable displacement from cubic. A possibility is the Fe^+ breaks the "d^0 rule" and continues to displace in the B-site of the cell. There are a few possible mechanisms toe account for this displacement [24] [25], but the existence of a tetragonal phase of PTFO, with the ferromagnetic Fe^{3+} in some of the B-cation sites, indicates its potential as a multiferroic material.

Chapter 3

Preparation of Bulk PbTiO$_3$ Samples and Hysteresis

3.1 Experimental Setup

3.1.1 Pelletization

The Precision LC loop tracer from Radiant Technologies is used to characterize the PbTi$_{1-x}$Fe$_x$O$_3$ samples. To produce samples for analysis in the looptracer, powder produced in the sol gel process detailed in Chapter 2 is compressed into small pellets about 2mm in diameter. 0.1-0.3 g of powder is compressed at 6-8 tn of pressure in a hand press into pellets. The pellets are sintered in atmosphere at around $650°C$ for 8-16 hours. I experimented extensively with the parameters of fabricating these pellets in order to produce durable and consistent samples. The process which was found to yield the highest quality pellets is as follows: 0.3g of PbTi$_{1-x}$Fe$_x$O$_3$ powder is pressed at 6tn

of pressure in a cylindrical chamber of about 2mm diameter for 2 hours. 3-5 drops of proponol or methanol is added to the powder in the chamber prior to pressing to help the powder shift and settle under pressure. The chamber has an air valve which allows gas to escape as the sample is compressed. Immediately after being removed from the press, the pellet is placed in a tube furnace to be sintered. The furnace increases temperature at a rate of $5°C/$min until reaching its target temperature of $650°$ C at atmosphere. The pellet remains at the target temperature for 8 hours, after which the oven is allowed to slowly cool back down to room temperature. The cooling process typically takes about 3 hours. Figure 3.1 shows examples of several pellets of various nominal iron concentrations produced with this method. Higher sintering temperatures increases the pellet hardness. There is also literature evidence that sintering temperature affects the polarization susceptibility; polarization is seen to decrease at sintering temperatures at $1000°$ [26].

In order to maximize the contact area, an electrode is added to the pellet. Placing small copper disks or pressing gold foil onto the face of the pellet is an easy way to add an electrode onto the pellet. However, to produce electrodes of uniform thickness and area and to ensure a consistent contact with the pellet, a more precise method of depositing electrodes is needed. Electron beam physical vapor deposition (EBPVD) is a good canidate for adding such high quality electrodes. Prelminiary trials depositing aluminum electrodes on sample pellets using a deposition chamber have produces ideal electrodes. It is likely that EBPVD will be the standard method of applying electrodes for future experiments with these PTFO pellets.
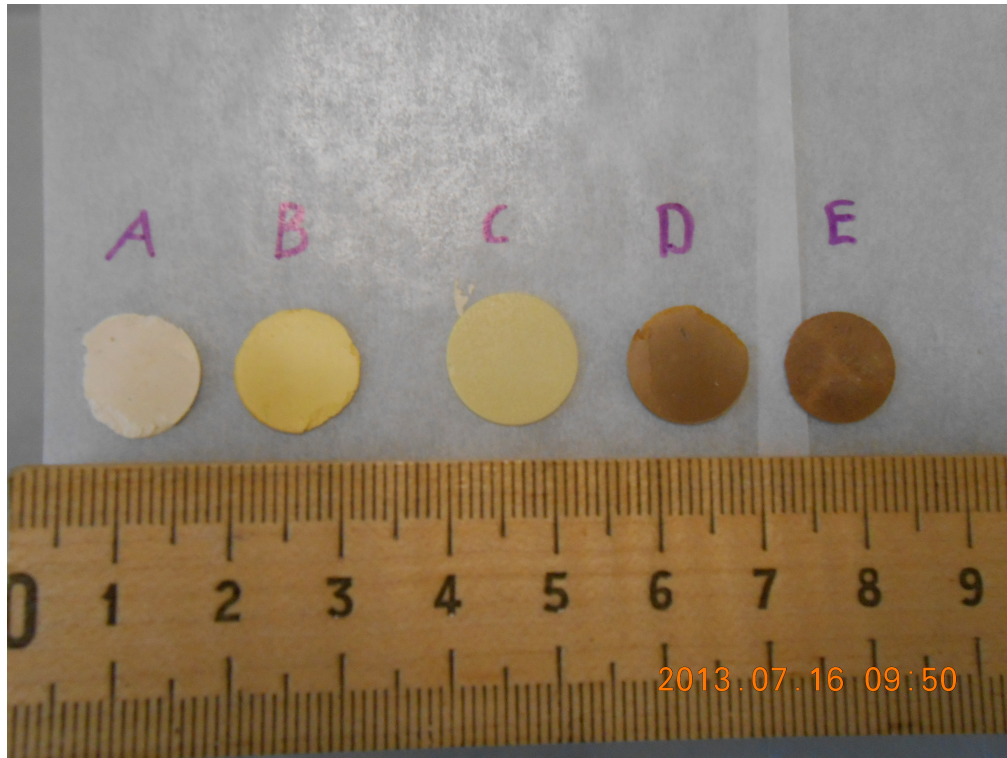
FIGURE 3.1: Pellets of $PbTi_{1-x}Fe_xO_3$: (A) $x = 0$, (B) $x = 0.05$, (C) $x = 0.1$, (D) $x = 0.3$ and (E) $x = 0.5$. The coloration of the pellets ranges from a pale yellow to dark reddish-brown as Fe concentration increases.

Even after sintering, the pellets remain fragile and prone to flaking. Note the flaked edges around samples (A), (B) and (D) in 3.1.

3.1.2   Ferroelectric Looptracing

The Precision LC looptracer (Figure 3.2) is a general purpose tester suitable for characterizing bulk ferroelectric ceramics. The tester has an output range of ±200V.

To measure ferroelectric hysteresis, a stimulus voltage loop is applied to the sample, and the charge produced is measured. The waveform of the applied voltage is triangular, as shown in figure 3.4. In fact, two loops are applied to a sample; a preset loop and a measurement loop. The preset loop is necessary because the state of polarization in

FIGURE 3.2: The Precision LC tester [2]. Not shown is the external testing bay that connects to the drive and return ports on the front of the tester.

a ferroelectric is unknown until the measurement is made. The first loop presets the polarization of the sample to a known state, which is then measured by the measurement loop.[27]
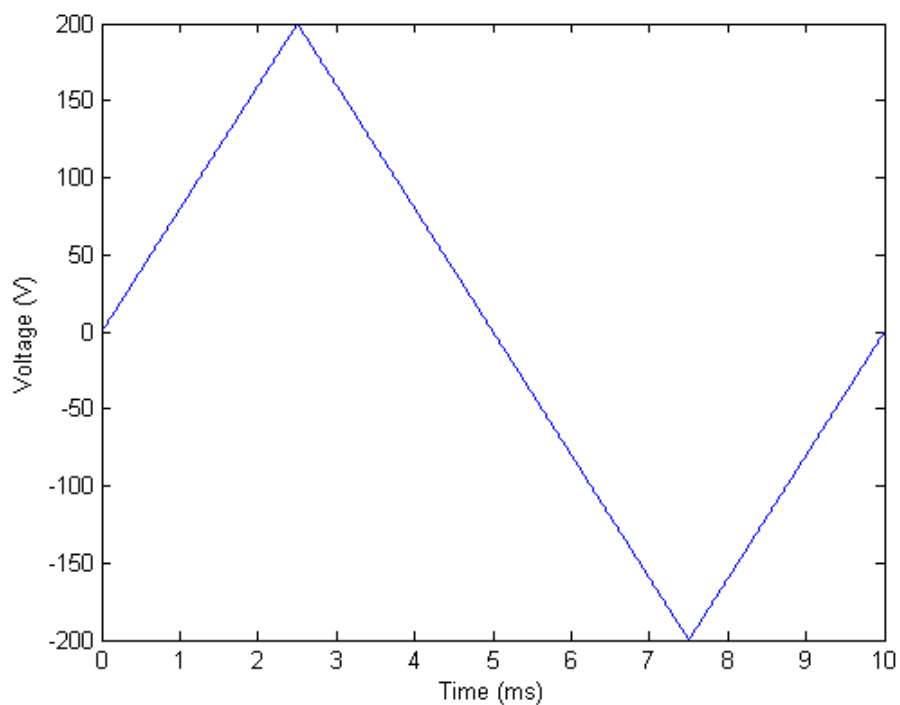

FIGURE 3.3: A triangular voltage waveform with period 10 ms. Two loops of this profile are applied for each polarization measurement.

Remnant hysteresis measurments are the preferred way to measure remnant polarization

in a ferroelectric. This is a two-pronged measurement: the hysteresis from an unswitched measurement loop and the hysteresis from a switched measurement loop are taken. The difference between these loops gives $2P_r$.
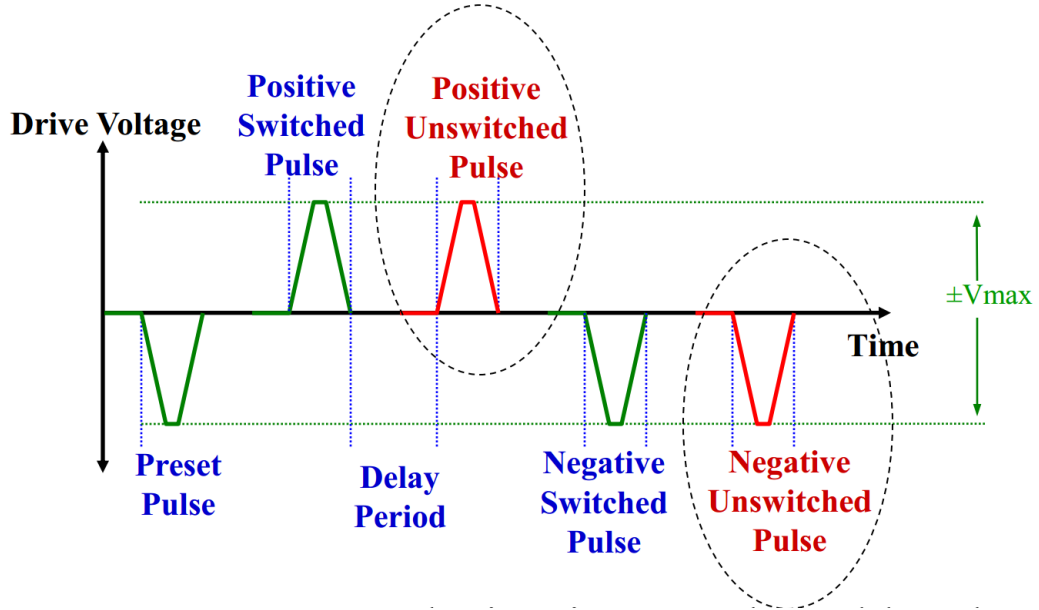

FIGURE 3.4: The wave form for measuring remnant polarization. The unswitched pulses are circled. The response from those pulses are subtracted from the response from the switched pulses to caculate remnant polarization. Figure produced by [3]

3.2 Results and Discussion

Although the 200V source on the Precision LC is inadequate to produce a switching voltage in the sample pellets, peliminary data on a few pellets, including results produced in the Radiant Technology laboratory with a 600V source have been produced. These results clearly show the presence of ferroelectricity in our $PbTi_{1-x}Fe_xO_3$ pellets, although more work is required to quantify the polarization and switching voltages for these pellets. Specifically analysis of thickness and surface contact via scanning electron microscopy is essential to normalizing the polarization shown in the following graphs.
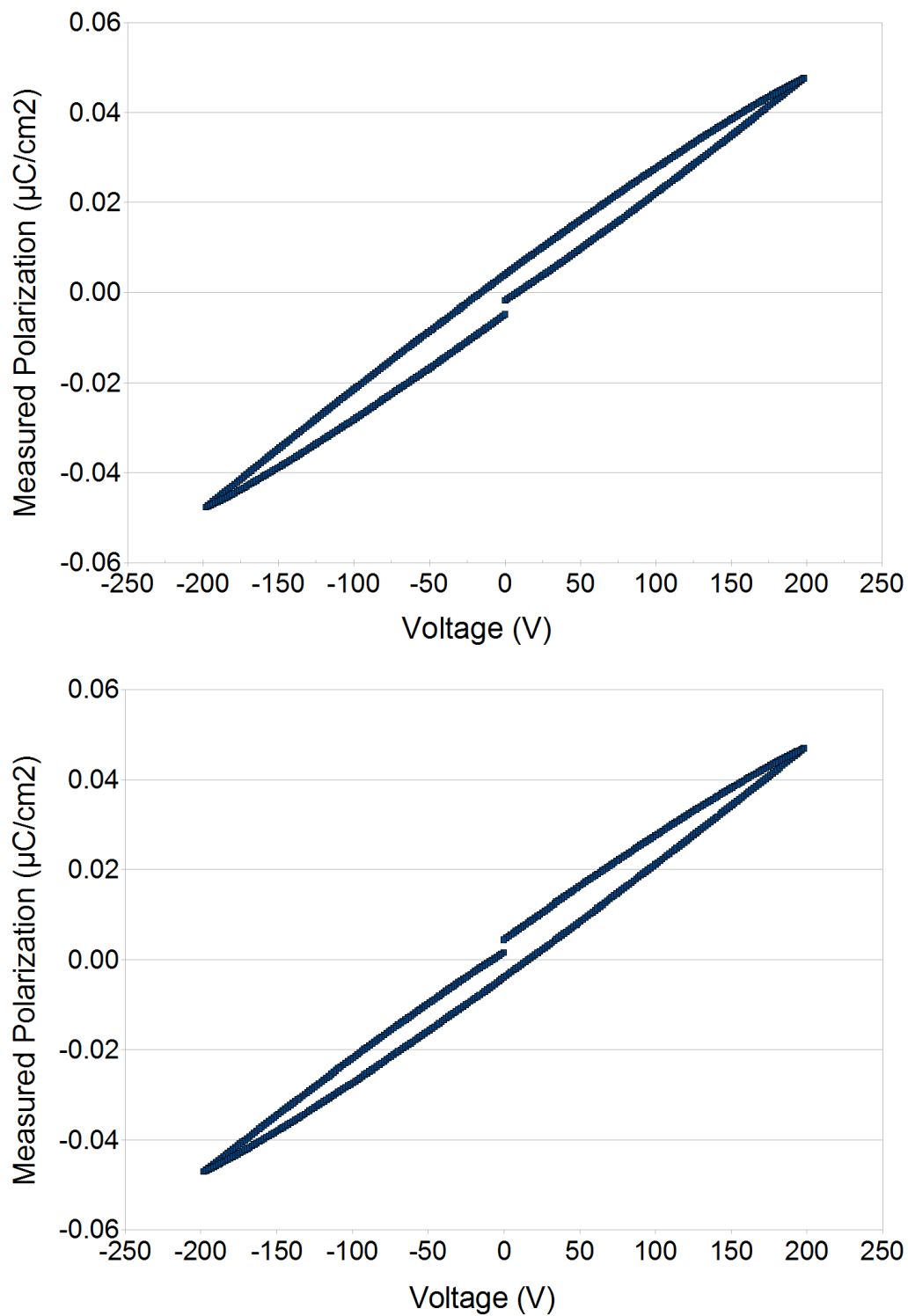
FIGURE 3.5: Polarization measurements of a 0.1g pellet of PTFO $x = 0.05$. Pellet thickness is estimated at 1mm, and contact area at 1cm^2. (a) hysteresis is traced counterclockwise, from positive voltage to negative. (b) is traced clockwise.
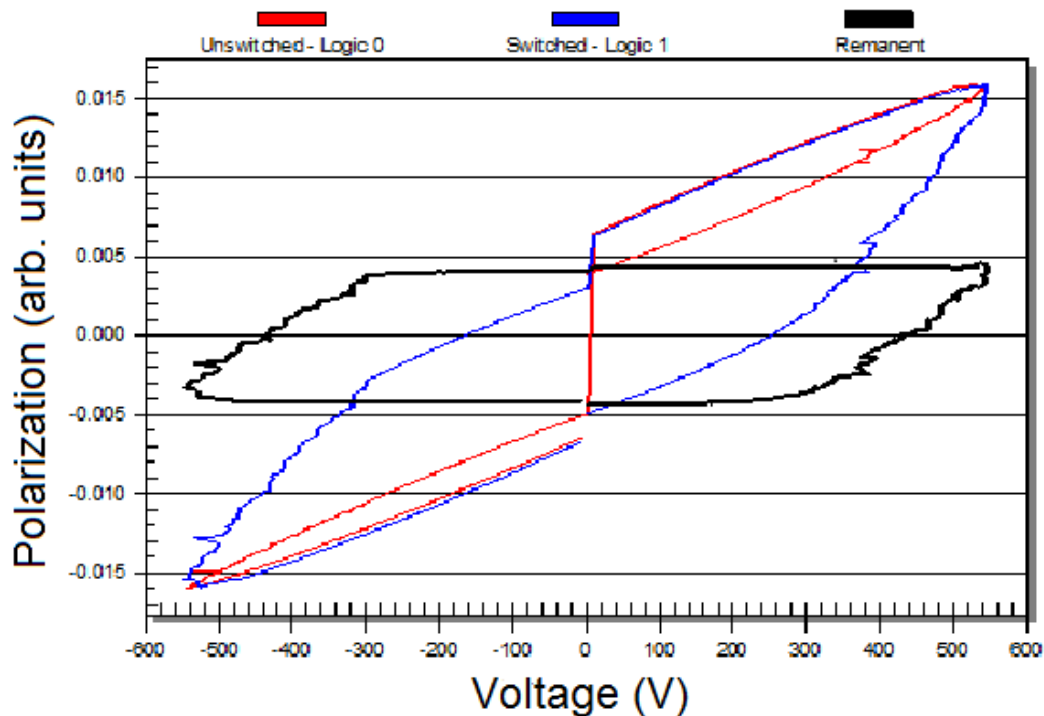
FIGURE 3.6: Remnant hysteresis results on a 0.1g pellet of PTFO $x = 0.1$ clearly showing the presence of remnant polarization. The sharp horizontal spikes are due to short-lived shorts in the pellet, possibly due to defects. Data produced by internal testing of the sample pellets by Joe Evans at Radiant Technologies, Inc.

3.5 demonstrates the dielectric response of $x = 0.05$ PTFO. The hysteresis curve is is characteristic of a lossy resistor [27]. This is likely due to multiple shorts in the pellet from a highly defective ceramic structure. No remnant polarization is seen in the hysteresis curves. The likely reason for this is the maximum voltage applied by the looptracer is 200V, probably below the switching current for the pellet. However, the "gap" seen in the curve in the starting and ending polarization of the ceramic is evidence of ferroelectricity. If the sample was merely a lossy dielectric, the hysteresis curve would be closed. Leakage currents are known to cause loss of polarization in $PbTiO_3$ [28]. The gap in 3.5 is likely due to the decay of remnant polarization during the testing of the sample through leakage currents.

The remnant hysteresis shown in 3.6 shows a clear polarization in the $x = 0.1$ pellet. The units of polarization is nominally $\mu m/cm^2$, but the testing bed electrode has an unclear surface area due to a rounded tip. I've chosen a reasonable are of $0.5 cm^2$, however these results should be treated as peliminary.

3.3   Conclusion

Pellets of $PbTi_{1-x}Fe_xO_3$ have been produced and shown to be ferroelectric. Looptracing measurements of $x = 0.05$ and $x = 0.1$ samples suggest a high defect structure. The main impediment to high quality polarization measurements on our samples is the fabrication of resilient pellets with high-quality electrodes. As 3.6 shows, the switching voltage of these samples is near $600V$. The leakage currents present in the sample are of concern, but should be mitigated by larger, higher quality electrode contacts on the pellets. EBPVD using aluminum or even platinum is the most promising method of attaching such electrodes.

Despite the shortcomings in sample quality, a ferroelectric polarization loop was obtained for the $x = 0.05$ sample.

Further work on these pellets is required to fully characterize their ferroelectric properties. Higher quality samples with larger contact areas will likely result in much higher quality measurements of ferroelectricity in PTFO. Further research is required to determine the effect of Iron doping in lead titanate.

Bibliography

[1] Ronald E. Cohen. Origin of ferroelectricity in perovskite oxides. *Nature*, 358:136–138, July 1992.

[2] Radiant technologies. http://www.ferrodevices.com/1/297/lc.asp. Accessed: 2013-8-21.

[3] Joe T. Evans. Characterizing ferroelectric materials. Technical report, Radiant Technologies, Inc., March 2011.

[4] Nicola A. Hill. Why are there so few magnetic ferroelectrics? *The Journal of Physical Chemistry B*, 104(29):6694–6709, 2000. doi: 10.1021/jp000114x.

[5] R. E. Cohen. Origin of ferroelectricity in perovskite oxides. *Nature*, 358:136–138, 1992.

[6] B. T. Matthias. New ferroelectric crystals. *Physical Review*, 75(11):1771, 1949.

[7] A.F. Devonshire. *Adv. Phys.*, 3:85, 1954.

[8] Mehran Kardar. *Statistical Physics of Particles*. Cambridge University Press, 1st edition, 2007.

[9] M.E. Lines and A.M. Glass. *Principles and Applications of Ferroelectrics and Related Materials.* Oxford University Press, 1977.

[10] P.W. Forsbergh. *Phys. Rev. B*, 93(686), 1954.

[11] L. Despont, C. Koitzsch, F. Clerc, M. G. Garnier, P. Aebi, C. Lichtensteiger, J.-M. Triscone, F. J. Garcia de Abajo, E. Bousquet, and Ph. Ghosez. Direct evidence for ferroelectric polar distortion in ultrathin lead titanate perovskite films. *Phys. Rev. B*, 73:094110, Mar 2006. doi: 10.1103/PhysRevB.73.094110. URL http://link.aps.org/doi/10.1103/PhysRevB.73.094110.

[12] Hui Wang and J. G. Che. A route to multiferroics by non-d 0 cation b in magnetic perovskites. *EPL (Europhysics Letters)*, 96(6):67012, 2011. URL http://stacks.iop.org/0295-5075/96/i=6/a=67012.

[13] N.A. Spaldin and M Fiebig. X-ray and neutron diffraction study of ferroelectric $PbTiO_2$. *Acta Crystallographica*, 9(2):131–140, Feb 1956. doi: 10.1107/S0365110X56000309.

[14] B. Noheda et al. *App. Phys. Lett.*, 74(2059), 1999.

[15] Kwangbae Lee, Byung Roh Rhee, and Chanku Lee. Characteristics of ferroelectric pb(zr,ti)o[sub 3] thin films having pt/pto[sub x] electrode barriers. *Applied Physics Letters*, 79(6):821–823, 2001. doi: 10.1063/1.1391226. URL http://link.aip.org/link/?APL/79/821/1.

[16] K. Shishir Ray. Growth and studeis of magnetoelectric multiferroic complex oxides. August 2010.

[17] C.H. Park and D.J. Chadi. Microscopic study of oxygen-vacancy defects in ferroelectric perovskites. *Physical Review B*, 57(22):961–964, June 1998.

[18] Leonid A. Bendersky and Frank W. Gayle. Electron diffraction using transmission electron microscopy. *Journal of Research of the National Institute of Standards and Technology*, 106(6), 2001.

[19] David B Williams and Barry C. Carter. *Transmission Electron Microscopy*. Springer Science + Business Media, 1st edition, 2009.

[20] Lone-Wen Tai and Paul A. Lessing. Modified resin-intermediate processing of perovskite powders: Part i. optimization of polymetric precursors. *Journal of Materials Research*, 7(2), 1992.

[21] G. Shirane, J. D. Axe, J. Harada, and J. P. Remeika. Soft ferroelectric modes in lead titanate. *Phys. Rev. B*, 2:155–159, Jul 1970. doi: 10.1103/PhysRevB.2.155. URL http://link.aps.org/doi/10.1103/PhysRevB.2.155.

[22] J.P. Remeika and A.M. Glass. The growth and ferroelectric properties of high resistivity single crystals of lead titanate. *Materials Research Bulletin*, 5(1):37 – 45, 1970. ISSN 0025-5408. doi: http://dx.doi.org/10.1016/0025-5408(70)90071-1. URL http://www.sciencedirect.com/science/article/pii/0025540870900711.

[23] J. C. Lodder and K. G. v.d. Berg. A method for accurately determining lattice parameters using electron diffraction in a commercial electron microscope. *Journal of Microscopy*, 100(1):93–98, 1974. ISSN 1365-2818. doi: 10.1111/j.1365-2818.1974. tb03916.x. URL http://dx.doi.org/10.1111/j.1365-2818.1974.tb03916.x.

[24] Isaac Bersuker. Pseudo jahn-teller origin of perovskite multiferroics, magnetic-ferroelectric crossover, and magnetoelectric effects: The d^0-d^{10} problem. *Phys. Rev. Lett.*, 108:137202, Mar 2012. doi: 10.1103/PhysRevLett.108.137202. URL http://link.aps.org/doi/10.1103/PhysRevLett.108.137202.

[25] I B Bersuker. A local approach to solid state problems: Pseudo jahn-teller origin of ferroelectricity and multiferroicity. *Journal of Physics: Conference Series*, 428 (1):012028, 2013. URL http://stacks.iop.org/1742-6596/428/i=1/a=012028.

[26] Guo-Long Tan Min Wang and Qingjie Zhang. Multiferroic properties of nanocrystalline pbtio3. *J. Am. Ceram. Soc.*, 93(8):2151 – 2154, 2010.

[27] M. Stewart and M.G. Cain. Ferroelectric hysteresis measurement & analysis. Technical report, National Physical Laboratory.

[28] A. Morelli, Sriram Venkatesan, G. Palasantzas, B. J. Kooi, and J. Th. M. De Hosson. Polarization retention loss in pbtio3 ferroelectric films due to leakage currents. *Journal of Applied Physics*, 102(8):084103, 2007.